Available online at www.sciencedirect.com
SCIENCE DIRECT®
Journal of Petroleum Science and Engineering 39 (2003) 217–230
JOURNAL OF PETROLEUM SCIENCE & ENGINEERING
www.elsevier.com/locate/jpetscieng

Use of X-ray computed microtomography to understand why gels reduce relative permeability to water more than that to oil

R.S. Seright[a,*], J. Liang[b], W. Brent Lindquist[c], John H. Dunsmuir[d]

[a] New Mexico Technology Petroleum Recovery Research Center, 801 Leroy Place, Socorro, NM 87807, USA
[b] Idaho National Engineering and Environmental Laboratory, ID, USA
[c] State University of New York at Stony Brook, Stony Brook, NY, USA
[d] ExxonMobil Research and Engineering Company, USA

Received 12 March 2002; received in revised form 13 September 2002

Abstract

X-ray computed microtomography (XMT) was used to investigate why gels reduce relative permeability to water more than that to oil in strongly water-wet Berea sandstone. XMT allows saturation differences to be monitored for individual pores during various stages of oil, water, and gelant flooding. The method also characterizes distributions of pore size, aspect ratio, and coordination number for the porous media. We studied a Cr(III) acetate–HPAM gel that reduced permeability to water (at S_{or}) by a factor 80–90 times more than that to oil (at S_{wr}). In Berea, the gel caused disproportionate permeability reduction by trapping substantial volumes of oil that remained immobile during water flooding (i.e., 43.5% S_{or} before gel placement versus 78.7% S_{or} after gel placement). With this high trapped oil saturation, water was forced to flow through narrow films, through the smallest pores, and through the gel itself. In contrast, during oil flooding, oil pathways remained relatively free from constriction by the gel.
© 2003 Elsevier Science B.V. All rights reserved.

Keywords: X-ray computed microtomography; Disproportionate permeability reduction

1. Introduction

Many polymers and gels can reduce the relative permeability to water more than that to oil or gas (Al-Sharji et al., 1999; Liang et al., 1992, 1995; Seright et al., 2002; Willhite et al., 2002; Zaitoun and Kohler 1991; Zaitoun et al., 1998). This property is critical to the success of water-shutoff treatments in production wells if hydrocarbon-productive zones cannot be protected during polymer or gelant placement (Liang et al., 1993; Seright et al., 1993). However, the magnitude of the effect has been unpredictable from one application to the next. Presumably, the effect would be more predictable and controllable if we understood why the phenomenon occurs. Although many mechanisms have been considered, the underlying cause of the disproportionate permeability reduction remains elusive.

Several authors used XMT to characterize the microscopic structure of porous media (Coles et al., 1996; Hazlett et al., 1996; Zhou et al., 2000). For a 15-darcy oil-wet sandstone, Coles et al. (1998)

* Corresponding author. Fax: +1-505-835-6031.
E-mail address: randy@prrc.nmt.edu (R.S. Seright).

0920-4105/03/$ - see front matter © 2003 Elsevier Science B.V. All rights reserved.
doi:10.1016/S0920-4105(03)00064-0

found a mean tortuosity of 2.7, with a range of 1.5–4.5. Along a 2.2-mm-long section of this core, porosity varied only a few percent around the average value (26.4%). Surprisingly, the water saturation only rose to 25.1% during oil flooding. Large variations in water saturation were observed along the 2.2-mm-long section—ranging from 12% to 39%. A three-dimensional view showed the non-wetting phase (water in this case) to exist as large ganglia (blobs of non-wetting phase that extend over multiple pores—often exhibiting a branched structure).

Using XMT data, Lindquist et al. (2000) extensively characterized pore and throat size distributions for Fontainebleau sandstones. As core porosity increased from 7.5% to 22%, the average pore coordination number increased from 3.4 to 3.8, the average channel length decreased from 200 to 130 μm, the average throat area increased from 1600 to 2200 μm^2, and the average pore volume remained fairly constant at around 0.0004 mm^3. The average aspect ratio (effective average pore radius/effective average throat radius) was around 2.

We used XMT to investigate why a Cr(IIII) acetate–HPAM gel reduces the relative permeability to water more than that to oil. This investigation provided interesting insights into distributions of pore sizes, aspect ratios, coordination numbers, and saturation distributions before and after gel placement in two Berea sandstone cores.

2. Experimental

In this paper, we describe imaging experiments using high-resolution computed X-ray microtomography (XMT) to compare the oil and water pathways and fluid distributions before and after gel treatment. The current generation of synchrotron-based XMT scanners provide the ability to obtain three-dimensional pore-level images of rock samples with a spatial resolution on the order of micrometers. For this study, we used the ExxonMobil beamline X2-B at the National Synchrotron Light Source (Dunsmuir et al., 1991; Flannery et al., 1987). X2-B is a dedicated XMT imaging facility capable of producing continuous registered stacks of $2048 \times 2048 \times 1024$ 14-bit three-dimensional images of X-ray linear attenuation coefficients at energies tunable from 8 to 40 keV. The highly collimated synchrotron X-rays permit the reconstruction of a three-dimensional image from two-dimensional projections taken at uniformly spaced angles between 0° and 180°. X2-B converts the pattern X-rays transmitted by the specimen (projections) to a visible light image using a thin single crystal of CsI(Na). This image was magnified by an optical microscope objective onto a 1024×1024 charge coupled device (CCD). Using Fourier methods, the set of angular projections at each row of pixels in the CCD was used to reconstruct the cross-sectional slice at that row. These slices were stacked to form the three-dimensional image. In this work, a $5\times$ microscope objective was used to provide a pixel size of 4.1-μm and a 4.1-mm field of view. Since part of the core was outside the imaged area, a profile extension method was used to suppress edge artifacts.

We performed two sets of imaging experiments using two strongly water-wet Berea sandstone cores (Cores A and B) with permeabilities of ~ 0.47 darcy and porosities of 22%. (Consistent porosity values were determined from both image analyses and conventional mass balance measurements.) The cores were 6.5 mm in diameter and 30 mm in length, with an intermediate pressure tap 6 mm from the inlet face. Our scans focused on a segment of the core that was 6.5 mm in diameter and 3.25 mm in length. To avoid end effects, the scanned segment was located about half way between the inlet and outlet faces. The brine used during the water floods contained 1% NaCl and 0.1% $CaCl_2$. A hexadecane mixture was used during the oil floods. To increase the image contrast between the brine and oil phases, hexadecane was doped with 10% w/w iodohexadecane in our first set of experiments (Berea Core A) and with 15% w/w bromohexadecane in the second set (Berea Core B). All experiments occurred at room temperature. The gelant used in these experiments contained 0.5% Alcoflood 935 HPAM (molecular weight $\approx 5 \times 10^6$ Da; degree of hydrolysis 5–10%), 0.0417% Cr(III) acetate, 1% NaCl, and 0.1% $CaCl_2$. The gelant viscosity at room temperature was 20 cp. The viscosities were 1.0 cp for brine (without polymer), 3.3 cp for the hexadecane/iodohexadecane mixture, and 3.6 cp for the hexadecane/bromohexadecane mixture.

3. Core flooding and characterization

The two Berea sandstone cores that were used in this work were first saturated with brine. Table 1 describes the sequences of oil, water, and gelant flooding for these cores.

Three-dimensional scans were performed after each flooding step indicated in Table 1. (Images were acquired at saturation endpoints.) All floods in a given set of experiments were conducted without removing the core from the sample stand so that the images could be compared directly. For each scan the image was cropped into a 2.97 × 2.97 × 2.1 mm rectangular block (the images were 725 × 725 × 512 voxels at 4.1 μm/voxel) to remove artifacts caused by those parts of the core that did not remain within the field of view through all 180° of sample rotation. Image analyses were performed using a software package called 3DMA—a statistical analysis tool that correlates saturations with geometry. This software is capable of measuring distributions of pore size, pore-body/pore-throat aspect ratio, and coordination number of a porous rock using our three-dimensional images. The methods used to make these characterizations are described by Lindquist et al. (2000).

3.1. Pore sizes

The imaged volumes included 1736 pores for Berea Core A and 1721 pores for Berea Core B. Distributions of pore volumes, aspect ratios, and coordination numbers for the Core A are shown in Fig. 1. For the pore volumes, the *y*-axis plots the percent of the total void volume that existed in pores with a given size (indicated on the *x*-axis). The peak in the pore volume occurred at an effective pore radius (assuming spherical pores) of about 50 μm (0.0005 mm^3) for Core A.

Table 1
Core flooding sequences

Flooding step	Berea Core A	Berea Core B
1	Saturated with brine	Saturated with brine
2	35 PV of oil	35 PV of oil
3	70 PV of brine	70 PV of brine
4	10 PV of gelant	35 PV of oil
5	20 PV of oil	
6	2.5 PV of brine	

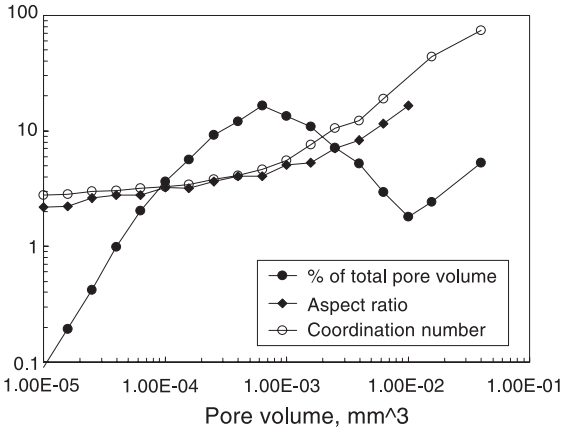

Fig. 1. Distribution of pore volumes, aspect ratios, and coordination numbers for Berea.

The average nodal pore volumes were similar to those found by Lindquist et al. (2000) for Fontainebleau sandstones (~ 0.0004 mm^3). Although many pores existed with volumes less than 0.0001 mm^3, their contribution to the total void volume was small.

3.2. Aspect ratios

The distribution of aspect ratios (effective pore radius/effective throat radius) are also shown in Fig. 1. (The effective pore radius assumed that the pore was spherical. The effective throat radius assumed that the throat area was circular.) The *y*-axis plots the average aspect ratio in pores with a given size (indicated on the *x*-axis). The average aspect ratio was 4.0/1. As pore volume increased from 10^{-5} mm^3 (effective pore radius ~ 13 μm) to 0.002 mm^3(effective pore radius ~ 78 μm), the average aspect ratio increased steadily from 2 to 6. Aspect ratios jumped sharply for the few largest pores. For a given pore size, a wide range of aspect ratios were noted. At a given pore size, the standard deviation (of aspect ratios) was typically 65% of the mean value. The average throat area was 1330 μm^2 for Core A. This value was generally lower than the average throat areas reported for Fontainebleau sandstones (1600–2200 μm^2—from Lindquist et al., 2000).

3.3. Coordination numbers

The distribution of coordination numbers for Core A are shown in Fig. 1. (The coordination number is the

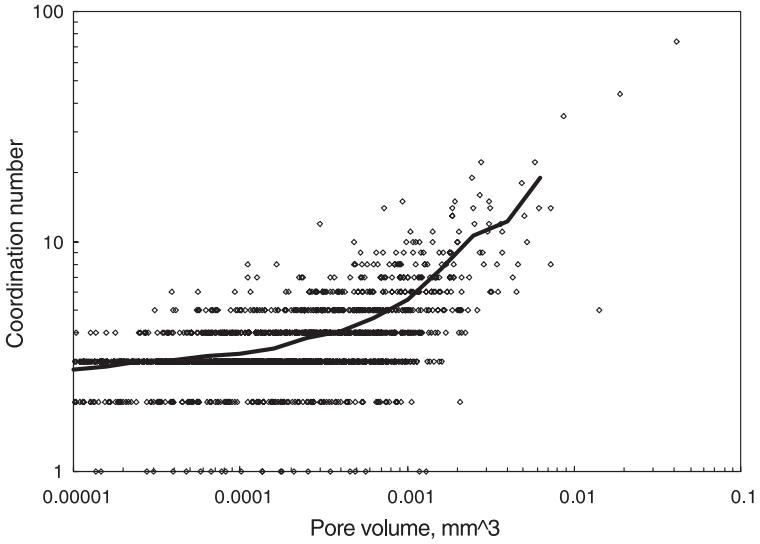

Fig. 2. Coordination numbers in Berea Core A: log scale.

number of exits from a pore.) The *y*-axis plots the average coordination number in pores with a given size (indicated on the *x*-axis). The average coordination number was 3.9 for Core A and 4.7 for Core B. For the smallest detected pores, the coordination number was around three for both cores. As the pore size increased, the average coordination number increased. In our first analysis, coordination numbers up to 74 were noted for the largest pores. For a given pore size, standard deviations were typically 20–40% of the mean values.

Ioannidis et al. (1997) reported comparable properties for Berea sandstone based on analyses of photomicrographs of 78 serial sections through a double

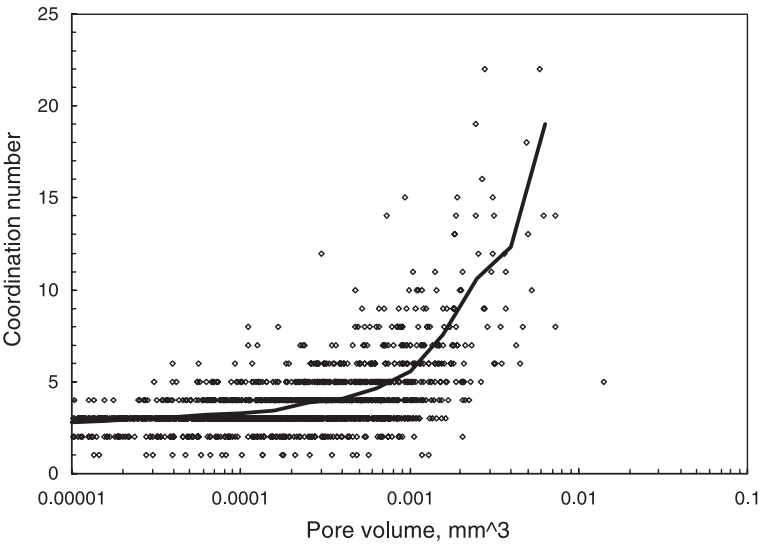

Fig. 3. Coordination numbers in Berea Core A: normal scale.

pore cast of a Berea sample. Their analyses of 1268 pores and 1945 throats indicated that the average coordination number was 3.46—somewhat lower than our values. Their average throat area was 60–90% greater than our values, and their pore size distribution was weighted toward larger pores than our distributions.

Some reviewers of our work were skeptical that coordination numbers could be as high as some of the values that we reported. In particular, M.A. Ioannidis (personal communication, Andover, NH, August 8, 2002) felt that coordination numbers should rarely be greater than 10. In view of these comments, we re-examined our data. Coordination numbers for individual pores in Core A are shown in Fig. 2 (log scale for the *y*-axis) and Fig. 3 (normal scale for the *y*-axis). In Fig. 2, only three pores had coordination numbers greater than 22.

Upon re-examination of the image analysis software (3DMA), we found that many pores were assigned extra throats that did not appear to connect to other pores. When these throats were eliminated, the largest coordination number for any pore decreased from 74 to 22. However, the average coordination number decreased only slightly—from 3.9 to 3.8. Fig. 4 plots the coordination numbers from the new analysis.

In the new analysis, the largest coordination number was 22. Detailed examination of the pore with the highest coordination number revealed that several of the throats led to the same pore. In one case, five throats connected the same two pores. In two cases, three throats connected the same two pores, and in one case, two throats connected the same two pores. These observations emphasize that the irregular shapes of the pore bodies and pore throats can complicate the analyses. If only one connection is allowed between any two pores, the maximum coordination number in Core A drops to 13.

Also, in the new analysis, six pores were identified with a coordination number of zero (no connection to other pores.) Other parameters (pore and throat sizes, aspect ratios, saturations) remained unchanged by the new analysis.

4. Analyses after the various floods

XMT scans were performed after each flood. Fluid saturations and permeabilities associated with the floods are listed in Table 2.

4.1. Before gelant injection

In Core A, the first scan viewed the core with 100% brine saturation. Second, the core was flooded with ~ 35 core pore volumes of oil and scanned at

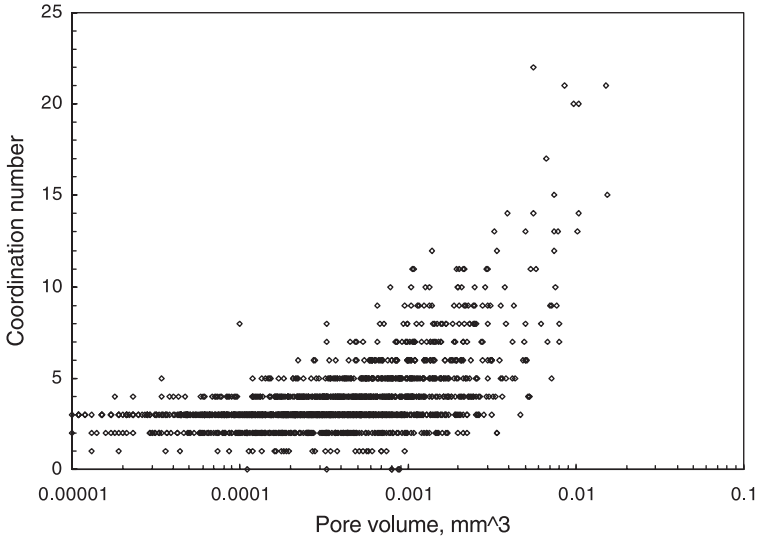

Fig. 4. Coordination numbers in Berea Core A: new analysis.

Table 2
Permeabilities, fluid saturations, and residual resistance factors

	Berea Core A	Berea Core B
Permeability (darcy)	0.47	0.48
Porosity (%)	22	22
S_w at first S_{wr} (%)	24.7	37.3
k_{ro} at first S_{wr}	0.82	0.79
S_w at first S_{or} (%)	56.5	56.8
k_{rw} at first S_{or}	0.16	0.18
S_w at second S_{wr} (%)		34.3
k_{ro} at second S_{wr}		0.78
S_w at first S_{or} after gel (%)	47.7	
S_w at S_{wr} after gel (%)	29.0	
F_{rro}	15	
S_w at second S_{or} after gel (%)	21.3	
F_{rrw}	1220	
F_{rrw}/F_{rro}	81	

residual water saturation. Oil invaded most pores while the residual water appeared dominantly in crevices and films between oil and the rock. The residual water saturation, S_{wr}, was 24.7% (Table 2), and the endpoint relative permeability to oil (relative to the absolute permeability), k_{ro}, was 0.82. Third, the core was flooded with water (~ 70 core pore volumes) and scanned at residual oil saturation. The residual oil occupied the centers of the pores while water formed a film around the residual oil. The residual oil saturation, S_{or}, was 43.5% (i.e., 100%–56.5%, from Table 2), and the endpoint relative permeability to water, k_{rw}, was 0.16. These findings are qualitatively consistent with expectations in a strongly water-wet rock.

Using the 3DMA software, detailed analyses were performed using the complete three-dimensional images. The distributions of water and oil saturations were determined as a function of pore size. In Fig. 5, the solid symbols show the distribution of water saturations (S_w) at S_{wr} before gel placement. (In this figure, average saturations for a given pore size are reported.) The open symbols show the distribution of water saturations at S_{or} before gel placement. (Of course, at any condition, the oil saturation is equal to 100% minus the water saturation.) The overall average S_{wr} of 24.7% was consistent with S_{wr} values measured using mass balances in this strongly water-wet Berea sandstone. As expected at S_{wr}, the water saturation generally increased with decreased pore size (solid circles in Fig. 5). A broad minimum in water saturation was noted around 0.002 mm^3, and a local maximum was observed around 0.01 mm^3. The significance of the increase in water saturation for the largest pores is debatable since only four pores were responsible for this increase.

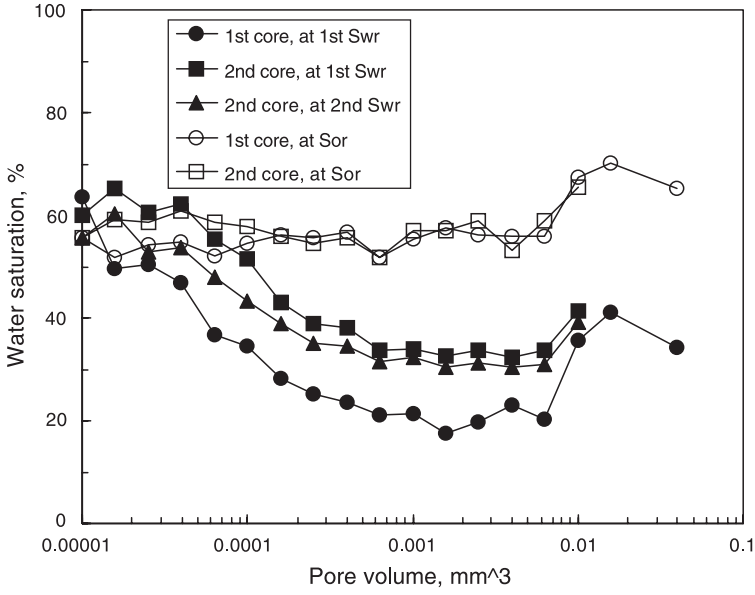

Fig. 5. Water saturations at S_{wr} and S_{or} before gel placement in Berea sandstone cores.

For a strongly water-wet porous medium, one might have expected the water saturation to approach 100% for the smallest pores shown. Instead, the water saturation in the smallest detected pores averaged 60%. A calculation using the Young–Laplace equation confirmed that oil should be able to enter the smallest pores that we detected in our Berea cores. Specifically, to enter the smallest detected pore throats (~ 7 μm radius), a capillary pressure around 1 psi was needed. This value was much lower than the 17 psi (pressure drop across the core) that was applied during our flooding experiments. (Of course, a 17-psi pressure drop across the core does not necessarily guarantee that the pressure drop across oil–water interfaces was greater than 1 psi.) The behavior of S_w versus pore size was confirmed during an imaging experiment in Core B (solid squares in Fig. 5). This experiment included a second oil flood (following an intervening water flood). Results from this part of the experiment (solid triangles in Fig. 5) further confirmed the above behavior during cycles of water and oil flooding before gel placement. The fluid saturations and relative permeabilities from Core B (Table 2) also showed fairly repeatable behavior during multiple flooding cycles.

The reader should recognize that pores with volumes of 10^{-5} mm^3 are not necessarily the smallest pores in our rock samples. Much smaller pores exist in clays and other minerals in Berea sandstone that are below the limits of detection for our XMT method. It seems likely that water saturations in these very small pores are nearly 100%. These observations may resolve the apparent discrepancy associated with very high water saturations being expected in the smallest pores. However, we should note that although pores smaller than 10^{-5} mm^3 exist, their contribution to the flow capacity of the rock is insignificant (Seright, 2001).

As mentioned, the overall average S_{or} was 43.5% for Core A. This number was significantly higher than the S_{or} values measured using mass balances in this strongly water-wet Berea sandstone (~ 22%). At S_{or}, the average water saturation was surprisingly insensitive to pore size (open circles in Fig. 5). The above results were confirmed during imaging studies of Core B (open squares in Fig. 5).

For a given pore size, Fig. 5 shows the average water saturation from a given experiment. However, for any given pore size, many pores were present, and a wide range of saturations was found. A detailed examination of the data revealed that for a given pore size, the range or distribution of water saturations was quite broad, both at S_{or} and at S_{wr}. At S_{or}, virtually all pores contained at least 20% oil and half the pores contained at least 45% oil.

One feature of these XMT studies is that we can monitor the saturation differences for individual pores from one flooding stage to the next. Figs. 6 and 7 plot these changes in water saturation for individual pores during oil and water flooding before gel placement. In these figures, the solid line plots the average change in water saturation for a given pore size. These solid lines are related to Fig. 5. For example, the solid line in Fig. 6 shows the difference between the open-circle curve (i.e., S_{or} for Core A) from the solid-circle curve (i.e., S_{wr} for Core A) in Fig. 5. Figs. 6 and 7 reveal that the average behavior results from a large variety of S_w changes that occur in individual pores. Fig. 7 is particularly revealing in this regard. Recall that viewing average behavior (Fig. 5) indicated similar behavior for the first and second S_{wr} conditions in Core B. Fig. 7 confirms that the saturation differences are certainly smaller than for other flooding transitions (i.e., Fig. 6). Nevertheless, significant pore-level saturation differences are evident—especially for the smaller pores (in Fig. 7).

4.2. During gelant injection

After establishing a residual oil saturation in Core A, the 20-cp Cr(III) acetate–HPAM gelant (10 core pore volumes) was injected using a pressure gradient of 17 psi/ft. After gel placement, the core was shut in for 12 h (at 60 °C) and scanned (at room temperature). The gelation time for this formulation was 1–1.5 h at 60 °C. Before gelation, the formulation was a homogenous solution which had the same viscosity as an HPAM solution with no crosslinker [i.e., the crosslinker in this case was Cr(III) acetate]. After gelation, the crosslinked polymer was an elastic semi-solid.

Fluid saturations changed somewhat during gelant injection—specifically, average water saturations decreased slightly in the medium to large pores during gelant injection (solid line in Fig. 8). Also, the overall average water saturation decreased from

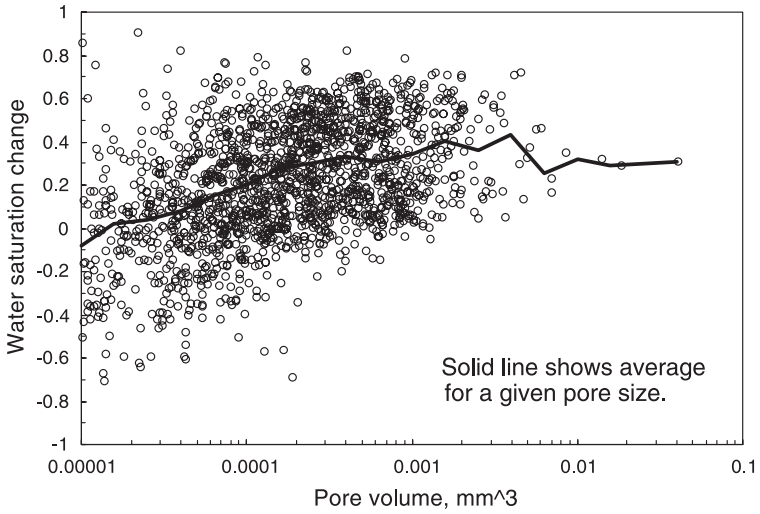

Fig. 6. S_w changes from S_{wr} to S_{or} for individual pores in Core A.

56.5% to 47.7% (Table 2). On first consideration, these observations surprisingly suggest that oil was generated when gelant (containing no oil) was injected. However, the reader should recall that the imaged volume constituted only 10% of the total core volume. Conceivably, oil was displaced from upstream portions of the core during gelant injection, and this oil became trapped in the imaged volume by coincidence. Presumably, the overall oil content of the core either stayed the same or decreased slightly during gelant injection. Fig. 8 confirms that many individual pores experienced saturation changes during the process of gelant injection.

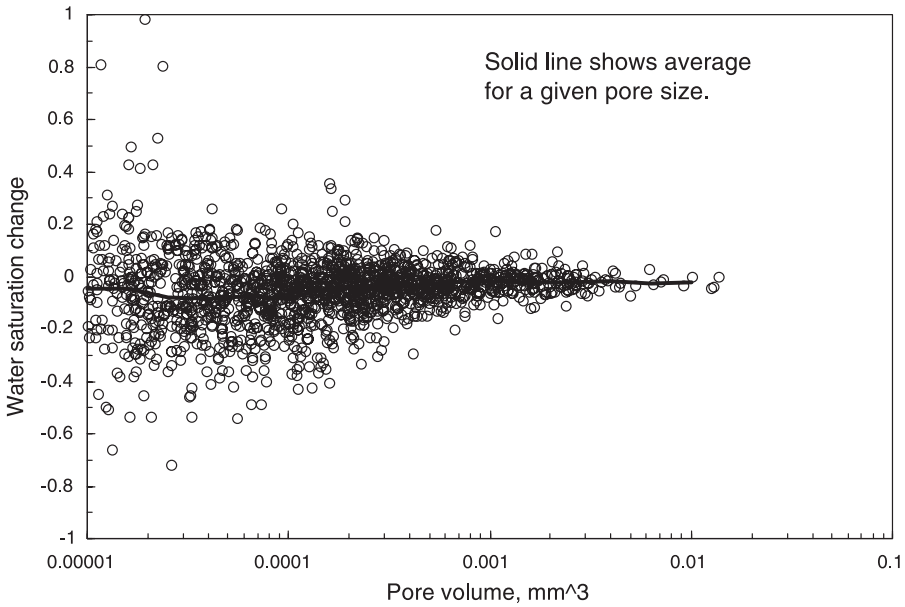

Fig. 7. S_w changes from first S_{wr} (37.3%) to second S_{wr} (34.3%) for individual pores in Core B.

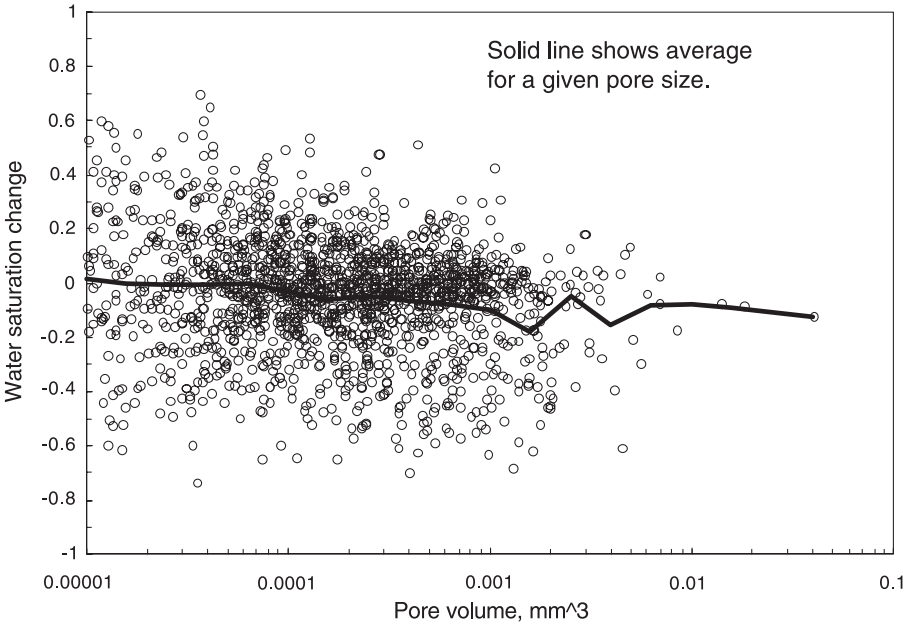

Fig. 8. S_w changes during gelant injection for individual pores in Core A.

4.3. After gel placement

After gel placement, oil (~ 20 core pore volumes) was injected to measure the oil residual resistance factor, F_{rro}—recording a value of 15. This value means that at S_{wr}, the gel reduced the permeability to oil by a factor of 15. The solid symbols in Fig. 9 compare distributions of water saturations at S_{wr} before versus after gel placement. The two distributions were remarkably similar, indicating that most

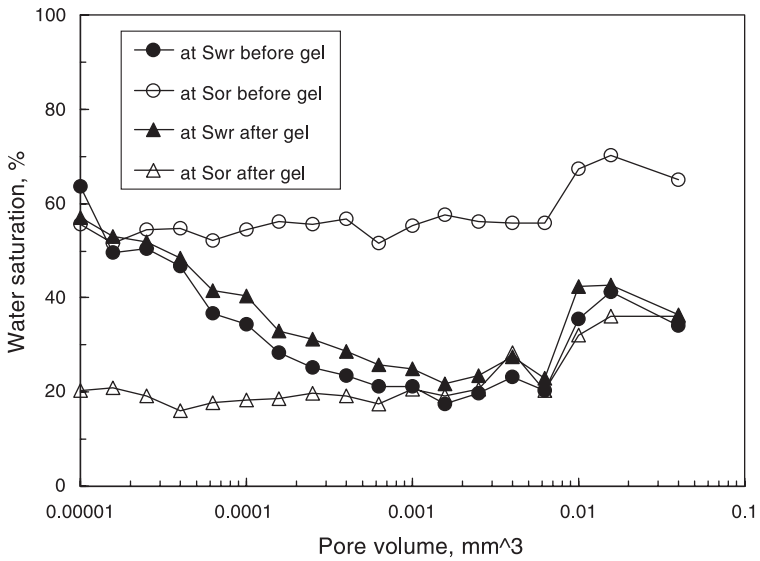

Fig. 9. Effect of gel on S_{wr} and S_{or} in Berea Core A.

of the pathways that were open to oil flow before gel placement were also open to oil flow after gel placement. This result suggests that the gel occupied only a small fraction of the pore space. This suggestion is consistent with the relatively low oil residual resistance factor (i.e., 15). Tracer results from a previous experiment in a high-permeability Berea core revealed that gel with an F_{rro} value of 20 occupied less than 5% of the pore space (Liang et al., 1992). Since the gel was placed and formed at high water saturation in the core, the result also suggests either (1) gel did not form in all the aqueous pore space (i.e., gelation was incomplete) or (2) oil flooding after gel placement moved, concentrated, or destroyed much of the gel that formed in the oil pathways.

Finally, brine (2.5 core pore volumes) was injected to measure the water residual resistance factor, F_{rrw}. The F_{rrw} value was 1220—meaning that at S_{or}, the gel reduced the permeability to water by a factor of 1220. This gel reduced the permeability to water 81 times more than that to oil ($F_{rrw}/F_{rro} = 81$).

At S_{or} after gel placement, water did not have access to most of the pathways that were open to oil flow after the gel treatment. The open symbols in Fig. 9 compare the distributions of water saturations at S_{or} before versus after gel placement. For reasons yet to be explained, water saturations in the smallest pores (< 0.0005 mm^3) at S_{or} after gel placement were less than those at S_{wr}. However, more importantly (because the total pore volume was dominated by the largest pores), the distribution of water saturations in the largest pores (>0.001 mm^3) after gel placement during water flooding (open triangles) was similar to that during the previous oil floods (solid symbols in Fig. 9). Therefore, the gel treatment apparently trapped substantial additional volumes of oil during water flooding (i.e., much higher S_{or} values). Perhaps, this result occurred because the gel was strategically positioned in pore throats to increase aspect ratios. With the larger pores permanently occupied by oil, water was forced to flow through narrow films, through the smallest pores, and through the gel itself—explaining the large water residual resistance factor (i.e., 1220). In contrast, oil pathways remained relatively free from constriction by the gel, so the oil residual resistance factor was much less (i.e., 15).

Saturation changes for individual pores during oil and water injection after gel placement are shown in Figs. 10 and 11. During oil injection after gel placement, a sizeable number of pores experienced very little saturation change (Fig. 10). Of course, many other pores gained in oil saturation. Very few

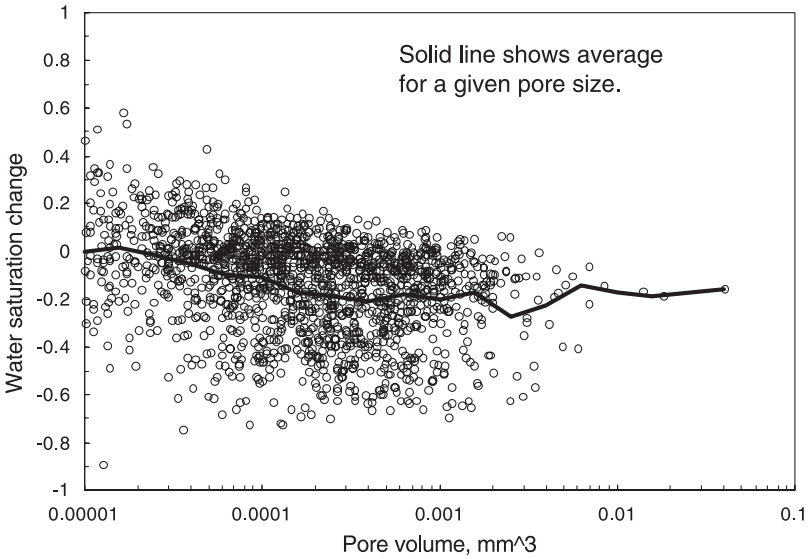

Fig. 10. S_w changes for individual pores in Berea during oil injection after gelation.

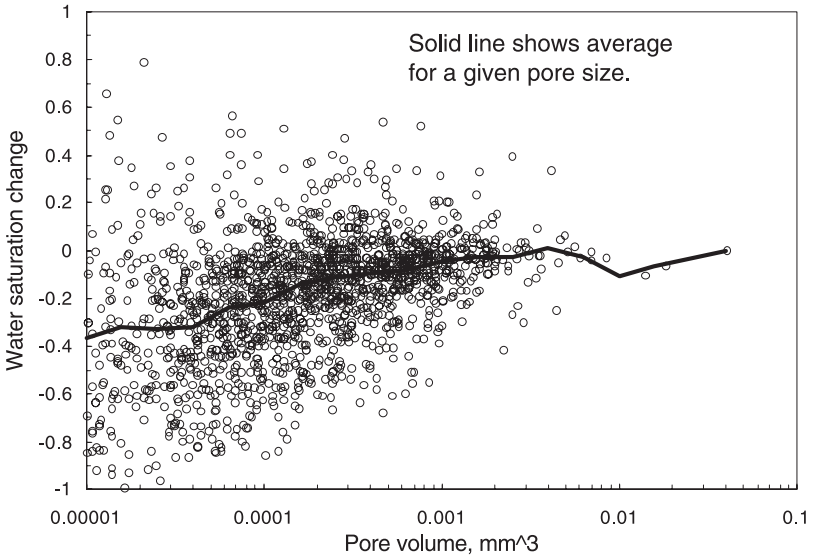

Fig. 11. S_w changes for individual pores in Core A during water injection after gelation.

pores gained significantly in water saturation. Fig. 10 was quite similar to that associated with the transition from S_{or} to S_{wr} before gel placement (Seright, 2001).

During water injection after gel placement (Fig. 11), many pores also experienced only small saturation changes. Many other pores experienced significant changes, with many gaining water while others gained in oil. The scatter in Fig. 11 suggests that a significant amount of saturation rearrangement occurred during water injection. The overall water saturation changed from 29.0% to 21.3%

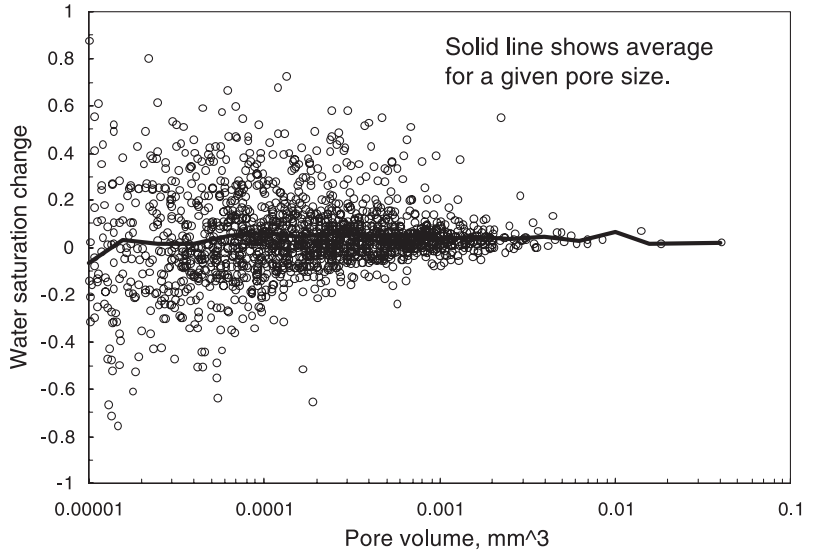

Fig. 12. S_w differences for individual pores in Core A at S_{wr} before (S_{wr} = 24.7%) versus after (S_{wr} = 29.0%) gel placement.

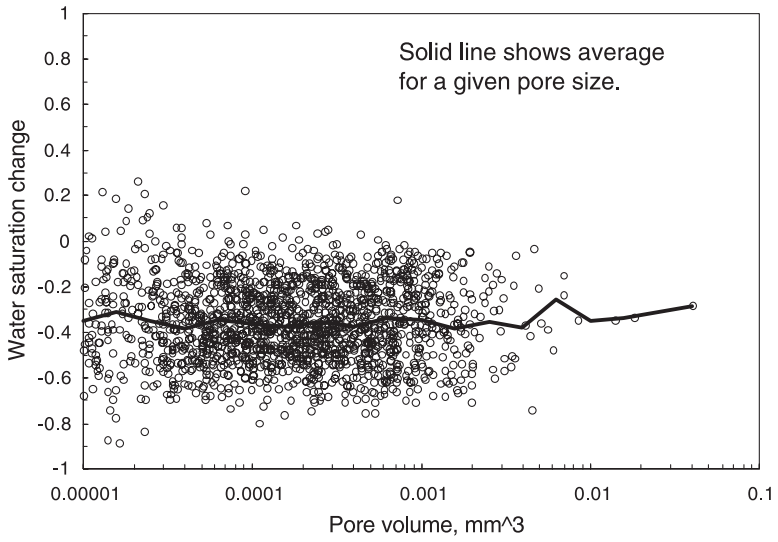

Fig. 13. S_w differences for individual pores in Core A at S_{or} before (S_{or} = 43.5%) versus after (S_{or} = 78.7%) gel placement.

(Table 2), suggesting that oil entered the image volume from other parts of the core during the displacement.

Fig. 12 compares saturation differences for individual pores before versus after gel placement when the core was at S_{wr}. As shown in Table 1, the S_{wr} was achieved by injecting 35 PV of oil before gel placement and 20 PV of oil after gel placement. Consistent with our earlier observations, at S_{wr}, most pores appeared to have about the same saturation after gel placement as before gel placement. This observation was most noticeable for the medium to large pores and was less valid for the smallest pores (i.e., those smaller than 10^{-4} mm^3).

Fig. 13 compares saturation differences for individual pores before versus after gel placement when the core was at S_{or}. This figure confirms that most pores (of all sizes) contained significantly more oil at S_{or} after gel placement than before gel placement. Thus, during water injection, the gel inhibited water flow by increasing the trapped oil saturation in most pores.

5. Relevance to field applications

In production wells where gelants were applied, some zones had high water saturations and high fractional water flows, while other zones had high hydrocarbon saturations and fractional flows. For the oil zones, the flooding sequence used for this paper mimics the field situation. Specifically, oil was the first fluid to flow through the gel after the treatment. Thus, the oil residual resistance factor of 15 and the mechanism for establishment of oil permeability through the gel are relevant to field applications (Liang et al., 1993; Seright et al., 1993). However, this is not the case for the water zones. Specifically, in water zones in field treatments, water was the first fluid to flow through the gel after gel placement—i.e., no oil flowed through the gel in the water zones. For this circumstance, our previous experience with Cr(III) acetate–HPAM gels revealed that water residual resistance factors were ~10,000 and the gel occupied virtually all of the aqueous pore space (Liang et al., 1992; Seright et al., 1993). Thus, the mechanism for water permeability reduction in field applications is actually one of near-total blockage of water flow. Virtually the only means for water flow is through the gel itself (which has a permeability less than 1 md) (Seright, 1996, 2001). In contrast, in the experiments here, the mechanism of water flow was examined after oil flowed through the gel. Nevertheless, since the water residual resistance factor in these experiments was 80–90 times greater than the oil residual resistance factor, the mechanism of relative permeability reduction for water is of scientific interest.

6. Conclusions

X-ray computed microtomography was used to investigate why gels reduce relative permeability to water more than that to oil in strongly water-wet Berea sandstone. The following conclusions were reached:

1. A Cr(III) acetate–HPAM gel reduced relative permeability to water by a factor 80–90 times more than that to oil.
2. In Berea, gel caused disproportionate permeability reduction by trapping substantial volumes of oil that remained immobile during water flooding. With this high trapped oil saturation, water was forced to flow through narrow films, through the smallest pores, and through the gel itself. In contrast, during oil flooding, oil pathways remained relatively free from constriction by the gel.

Nomenclature

F_{rr}	Residual resistance factor
F_{rro}	Residual resistance factor for oil
F_{rrw}	Residual resistance factor for water
k_{ro}	Relative permeability to oil
k_{rw}	Relative permeability to water
S_{or}	Residual oil saturation, %
S_w	Water saturation, %
S_{wr}	Residual water saturation, %

Acknowledgements

Financial support for this work is gratefully acknowledged from the National Petroleum Technology Office of the United States Department of Energy, BP, Chevron, China National Petroleum, Chinese Petroleum, Marathon, Shell, and Texaco. The efforts of John Hagstrom were appreciated during the corefloods and imaging experiments. We also thank Dr. Jill S. Buckley (New Mexico PRRC) for helpful discussions and suggestions. This research was carried out (in part) at the National Synchrotron Light Source, Brookhaven National Laboratory, which is supported by the U.S. Department of Energy, Division of Materials Sciences and Division of Chemical Sciences. The Geosciences Program of the U.S. Department of Energy (grant DE-FG02-92ER14261) funded development of the 3DMA code.

References

Al-Sharji, H.H., Grattoni, C.A., Dawe, R.A., Zimmerman, R.W., 1999. Pore-Scale Study of the Flow of Oil and Water Through Polymer Gels. 1999 SPE Annual Technical Conference and Exhibition, Houston, Oct. 3–6. Paper SPE 56738.

Coles, M.E., Hazlett, R.D., Spanne, P., Soll, W.E., Muegge, E.L., Jones, K.W., 1996. Pore Level Imaging of Fluid Transport Using Synchrotron X-ray Microtomography. International Symposium of the Society of Core Analysts, Montpellier, France, Sept. 8–10. Paper 9628.

Coles, M.E., Hazlett, R.D., Muegge, E.L., Jones, K.W., Andrews, B., Bowd, B., Siddons, P., Peskin, A., Spanne, P., Soll, W.E., 1998. Developments in synchrotron X-ray microtomography with applications to flow in porous media. SPEREE, 288–296.

Dunsmuir, J.H., Ferguson, S.R., D'Amico, K.L., Stokes, J.P., 1991. X-ray Microtomography: A New Tool for the Characterization of Porous Media. 1991 SPE Annual Technical Conference and Exhibition, Dallas, Oct. 6–9. Paper SPE 22860.

Flannery, B.P., Deckman, H.W., Roberge, W.G., D'Amico, K.L., 1987. Three-dimensional X-ray microtomography. Science 237, 1439.

Hazlett, R.D., Chen, S.Y., Soll, W.E., 1996. Wettability and Rate Effects on Immiscible Displacement: Lattice Boltzmann Simulation in Microtomographic Images of Reservoir Rocks. 4th International Symposium on Evaluation of Reservoir Wettability and its Effect on Oil Recovery, Montpellier, France, pp. 11–13.

Ioannidis, M.A., Kwiecien, M.J., Chatzis, I., Mcdonald, I.F., Dullien, F.A.L., 1997. Comprehensive Pore Structure Characterization Using 3D Computer Reconstruction and Stochastic Modeling. 1997 SPE Annual Technical Conference and Exhibition, San Antonio, Oct. 5–8. Paper SPE 38713.

Liang, J., Sun, H., Seright, R.S., 1992. Reduction of Oil and Water Permeabilities Using Gels. 1992 SPE/DOE Symposium on Enhanced Oil Recovery, Tulsa, April 22–24. Paper SPE 24195.

Liang, J., Lee, R.L., Seright, R.S., 1993. Placement of gels in production wells. SPEPF, 276–284 (Transactions 295).

Liang, J., Sun, H., Seright, R.S., 1995. Why do gels reduce water permeability more than oil permeability? SPERE, 282–286 (Nov. 1995).

Lindquist, W.B., Venkatarangan, A., Dunsmuir, J., Wong, T., 2000. Pore and throat size distributions measured from synchrotron X-ray tomography images of Fountainebleau sandstones. J. Geophys. Res. 105B, 21508–21528.

Seright, R.S., 1996. Improved Techniques for Fluid Diversion In Oil Recovery, final report, DOE/BC/14880-15, U.S. DOE, 97-108.

Seright, R.S., 2001. Using Chemicals to Optimize Conformance Control in Fractured Reservoirs, annual report, DOE/BC/15110-6, Contract No. DE-AC26-98BC15110, U.S. DOE.

Seright, R.S., Liang, J., Sun, H., 1993. Gel treatments in production wells with water coning problems. In Situ 17 (3), 243–272.

Seright, R.S., Liang, J., Lindquist, B.W., Dunsmuir, J.H., 2002. Characterizing Disproportionate Permeability Reduction Using Synchrotron X-ray Computed Microtomography. SPEREE, 355–364.

Willhite, G.P., Zhu, H., Natarajan, D., McCool, C.S., Green, D.W., 2002. Mechanisms Causing Disproportionate Permeability in Porous Media Treated With Chromium Acetate/HPAAM Gels. SPE J., 100–108.

Zaitoun, A., Kohler, N., 1991. Thin Polyacrylamide Gels for Water Control in High-Permeability Production Wells. 1991 SPE Annual Technical Conference and Exhibition, Dallas, Oct. 6–9. Paper SPE 22785.

Zaitoun, A., Bertin, H., Lasseux, D., 1998. Two-Phase Flow Property Modifications by Polymer Adsorption. 1998 SPE/DOE Improved Oil Recovery Symposium, Tulsa, April 19–22. Paper SPE 39631.

Zhou, M., Dalian, L., Dunsmuir, J., Thomann, H., 2000. Irreducible water distribution in sandstone rock: two-phase flow simulations in CT-based pore network. Phys. Chem. Earth (A) 25 (2), 169–174.